Journal of Catalysis 285 (2012) 251–259

Contents lists available at SciVerse ScienceDirect

Journal of Catalysis

journal homepage: www.elsevier.com/locate/jcat

Alkylphosphonic acid- and small amine-templated synthesis of hierarchical silicoaluminophosphate molecular sieves with high isomerization selectivity to di-branched paraffins

Yu Fan [a,b], Han Xiao [b], Gang Shi [b], Haiyan Liu [b], Xiaojun Bao [a,b,*]

[a] *State Key Laboratory of Heavy Oil Processing, China University of Petroleum, Beijing 102249, PR China*
[b] *The Key Laboratory of Catalysis, China National Petroleum Corporation, China University of Petroleum, Beijing 102249, PR China*

ARTICLE INFO

Article history:
Received 10 February 2011
Revised 22 September 2011
Accepted 27 September 2011
Available online 1 November 2011

Keywords:
Hierarchical silicoaluminophosphate
Alkylphosphonic acid
Mesopore
Isomerization

ABSTRACT

This article proposes a one-step strategy to hydrothermally synthesize SAPO-11 with hierarchical micro- and meso-porous structure. The structure and acidity properties and the isomerization performance of the resulting hierarchical SAPO-11 were extensively characterized and assessed, respectively, and compared with those of a microporous SAPO-11. The results showed that the SAPO-11 with mutually interpenetrating micropores and mesopores had been obtained by introducing tetradecylphosphoric acid into the synthesis system of microporous SAPO-11. Compared with microporous SAPO-11, the hierarchical SAPO-11 had much higher external surface and mesoporous volume, and more active sites with suitable Brönsted acid strength. These advantages endowed the hierarchical SAPO-11-based catalyst with superior isomerization activity, enhanced selectivity to di-branched products, and decreased cracking selectivity. The strategy proposed opens a new route to synthesizing a variety of hierarchical mesoporous SAPO molecular sieves for size-selective catalytic conversions of relatively large hydrocarbon molecules.

1. Introduction

Nowadays, microporous zeolites are being widely applied in petroleum refining and petrochemical industries as solid acid catalysts [1]. However, the predominant presence of micropores in microporous zeolites imposes diffusion limitations on reactions involving bulkier molecules that have the size larger than micropores [2,3]. To overcome this limitation, extensive efforts have been devoted to synthesis of zeolitic nanocrystals [4], large-pore zeolites and zeolitic analogs [5,6], and ordered mesoporous materials [7,8]. Unfortunately, the difficulty to separate zeolitic nanocrystals from the reaction mixture owing to their colloidal nature [4] and the obstacle to substantially improve the structural stability of large-pore zeolites and zeolitic analogs as well as ordered mesoporous materials hinder their practical application in industry [9]. It has been recognized that generation of mesopores in microporous zeolites is a feasible way to enhance the mass transfer of reactants and intermediate molecules to active centers [10], and for this purpose, various post-synthesis methods, such as steaming and chemical treatments, have been proposed, but they unavoidably lead to the decrease in zeolite crystallinity and the uncontrollable formation of mesopores, which can negatively influence the catalytic performance of zeolites [11]. Recently, the meso-scale template-directed routes to synthesizing micro–mesoporous aluminosilicate zeolites with high crystallinity and enhanced mass transfer have been proposed [12]. The used meso-scale templates include nano-structured carbons [13,14], polymers [15,16], biological templates [17], and organosilanes [18,19]. While various methods have been attempted to create mesopores in microporous aluminosilicate zeolites, little is known about the generation of mesopores in microporous silicoaluminophosphate (SAPO) molecular sieves that have wide applications for the conversion of hydrocarbons [20,21]. Like aluminosilicate zeolites, microporous SAPO also suffers mass transfer limitation in the conversion of hydrocarbons. For example, skeletal isomerization of high *n*-paraffins (C_7+), one of the most important processes in the modern petroleum refining industry, can dramatically improve the quality of various petroleum processing products such as gasoline, diesel, jet fuel and lubricating oil basestock. In these processes, microporous SAPO-11 with outstanding isomerization activity but lower cracking activity demonstrates significant advantages over microporous aluminosilicate zeolites, such as β, ZSM-5, and mordenite [22]. However, the one-dimensional pore size of 0.39 × 0.63 nm in SAPO-11 detrimentally restrains the formation of di-branched isomers that are more efficient in improving target product quality than mono-branched isomers [23]. Therefore, SAPO-11 with hierarchical pore structure is

---

* Corresponding author at: State Key Laboratory of Heavy Oil Processing, China University of Petroleum, Beijing 102249, PR China. Fax: +86 (0) 10 89734979.

E-mail address: baoxj@cup.edu.cn (X. Bao).

0021-9517/$ - see front matter © 2011 Elsevier Inc. All rights reserved.
doi:10.1016/j.jcat.2011.09.037

expected to enhance the formation of multi-branched isomers, conquering the shape-hindrance problem that universally exists in industrial isomerization processes.

In line with the above discussion, herein we present a one-step method to hydrothermally synthesize SAPO-11 with hierarchical micro- and meso-porous structure. This method is achieved by using a tetradecylphosphoric acid (TDPA) template for the first time to create mesopores and a conventional di-*n*-propylamine (DPA) template to create micropores. Isomerization of long-chain paraffins over the SAPO-11-based catalyst is selected as a model reaction to demonstrate the advantages of the resulting hierarchical SAPO-11 molecular sieve (H-SAPO-11-HI) for promoting the mass transfer and the catalytic selectivity. For comparison, a conventional microporous SAPO-11 (H-SAPO-11) only with conventional DPA as template was synthesized in the absence of alkylphosphonic acid by a similar procedure, and the isomerization performance of the corresponding catalyst was assessed.

2. Experimental

2.1. Synthesis of microporous SAPO-11

Microporous SAPO-11 was hydrothermally synthesized from a gel consisting of 1.2 di-*n*-propylamine (DPA):1.0 Al_2O_3:1.0 P_2O_5:0.3 SiO_2:120 H_2O in molar ratio. First, 12.4 g of phosphoric acid (85 wt%; Beijing Jinxing Chemical Plant, PR China) was dissolved in 115.9 g of deionized water under stirring, then 7.21 g of pseudoboehmite (76 wt% Al_2O_3; Tianjin Hengmeilin Chemical Co., PR China) was slowly added, and the obtained mixture was stirred for 2 h; second, 3.39 g of tetraethyl orthosilicate (99% TEOS; Beijing Chemical Reagent Co., PR China) was slowly added and stirred for 2 h; third, 6.58 g of DPA (99 wt%; Beijing Jinxing Chemical Plant, PR China) was added into the above mixture and stirred for 2 h; finally, the resulting homogenous gel was crystallized in a Teflon-lined stainless steel autoclave at 458 K for 48 h and then the solid product recovered by centrifugation was washed with deionized water, dried at 383 K for 3 h, and calcined at 873 K for 6 h to remove the template. The obtained sample was ion-exchanged three times with 1 M NH_4NO_3 (99%; Beijing Chemical Reagent Co., PR China) for 2 h at 353 K and calcined at 723 K for 4 h to give H-SAPO-11.

2.2. Synthesis of hierarchical SAPO-11

The synthesis procedure was analogous to the above procedure used for synthesizing the microporous SAPO-11 except that tetradecylphosphoric acid (TDPA; J & K Scientific Ltd., Beijing, PR China) was used as an additional template to generate mesopores. At the very beginning, 1.55 g of TDPA was added into 115.9 g of deionized water under stirring and then 7.21 g of pseudoboehmite was slowly added and stirred for 2 h. Then, 12.4 g of phosphoric acid was added into the above mixture and stirred for 1 h. The followed procedure was the same as that used for synthesizing the microporous SAPO-11. The molar composition of the resulting homogenous gel for synthesizing the hierarchical SAPO-11 was 0.1 TDPA:1.2 DPA:1.0 Al_2O_3:1.0 P_2O_5:0.3 SiO_2:120 H_2O. The template removal and the subsequent ion-exchange were performed according to the same steps described above. The obtained sample was named as H-SAPO-11-HI.

2.3. Catalyst preparation

Pt/H-SAPO-11 and Pt/H-SAPO-11-HI catalysts were prepared by the incipient wetness impregnation of the above calcined H-SAPO-11 and H-SAPO-11-HI of the size 20–40 mesh with an aqueous solution of hexachloroplatinic acid according to the required loading. After being dried at 383 K for 2 h and calcined at 723 K for 2 h, the oxidic catalysts were obtained. The Pt loading of the two catalysts determined by X-ray fluorescence spectroscopy (XRF) on a Rigaku ZSX-100e instrument was 1.0 wt%.

2.4. Characterizations

X-ray diffraction (XRD) analyses of the calcined samples were conducted on a Shimadzu XRD-6000 diffractometer that uses Cu Kα radiation and is operated at 40 kV and 30 mA with 2θ scanning speed at 4 deg/min and diffraction lines of 2θ between 5° and 50°.

Scanning electron microscopy (SEM) images of the calcined samples were obtained on a LEO 1530 Gemini instrument (Zeiss) operated at 1 kV. The sample was deposited onto a conductive carbon foil supported on an aluminum stub.

High-resolution transmission electron microscopy (HRTEM) images of the calcined samples were obtained on a Philips CM30 microscope with a point resolution of 0.2 nm at 300 kV. The sample was ground, dispersed in ethanol, and deposited on a holey carbon film supported on a copper grid.

Nitrogen adsorption–desorption measurements were performed on a Micromeritics ASAP 2405N adsorption instrument. The calcined samples were degassed at 573 K in a vacuum of 1.33×10^{-3} Pa for 15 h and then switched to the analysis station for adsorption–desorption at liquid nitrogen temperature.

^{27}Al magic-angle spinning nuclear magnetic resonance (^{27}Al MAS NMR) experiments of the calcined samples were carried out on a Bruker Avance 700 NMR spectrometer using a 2.5-mm double-resonance probe head. The resonance frequency for ^{27}Al was 182.4 MHz, the pulse length was 6 μs, and the recycle delay was 1 s. All spectra were obtained at a spinning speed of 15 kHz. The ^{27}Al chemical shifts were referenced to alum ($(NH_4)Al(SO_4)_2 \cdot 12H_2O$). ^{29}Si and ^{31}P MAS NMR measurements of the calcined samples were performed on a Bruker Avance 500 NMR spectrometer using a 4-mm probe head. For ^{29}Si MAS NMR, a spinning frequency of 8 kHz and a relaxation delay of 5 s were employed. The ^{29}Si chemical shifts were referenced to octakis-(trimethylsiloxy) silsesquioxane. To record the ^{31}P MAS NMR spectra, a spinning frequency of 8 kHz and a relaxation delay of 1 s were employed. The field was calibrated by measuring the ^{13}C MAS NMR spectra of glycine.

The infrared (IR) spectra were measured on a MAGNA-IR 560 Fourier transformed IR (FT-IR) instrument (Nicolet Co., America) with a resolution of 1 cm^{-1}. The self-supported wafers of the uncalcined samples were evacuated in situ in an IR cell at 623 K for 4 h, and IR spectra were recorded after the temperature was decreased to room temperature.

The pyridine-adsorbed IR (Py-IR) measurements were performed on the same MAGNA-IR 560 instrument used for the above FT-IR measurements. The self-supported wafers of the calcined samples were dehydrated at 773 K for 5 h under a vacuum of 1.33×10^{-3} Pa, followed by the adsorption of pure pyridine vapor at room temperature for 20 min; then, the system was evacuated at different temperatures and Py-IR spectra were recorded.

The thermogravimetry (TG) measurements of the uncalcined samples were performed on a Netzsch STA 409PC thermogravimetric analyzer at a heating rate of 5 K/min.

The dispersion of metal Pt on the catalysts was determined by H_2 adsorption using a classical volumetric apparatus. The dispersion of Pt was calculated by assuming that each surface Pt atom chemisorbs one hydrogen atom.

2.5. Catalyst assessment

n-Octane isomerization was conducted in a continuously flowing tubular fixed-bed microreactor at 1.5 MPa. 0.60 g of the catalyst to

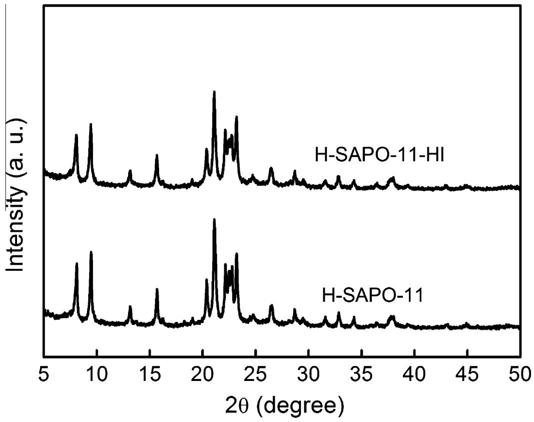

Fig. 1. XRD patterns of the calcined H-SAPO-11 and H-SAPO-11-HI molecular sieves.

be assessed was diluted with quartz particles of 0.25 mm in diameter to a constant volume of 2.0 mL before being loaded into the reactor. Prior to the reaction, the catalysts were treated in situ at 723 K in air for 2 h to purge their surface, followed by reduction in H_2 at 623 K for 2 h to reduce Pt^{II} to metal Pt. The catalysts were tested at 593 K, a volumetric H_2/octane ratio of 400, and different weight hour space velocities (WHSVs). After steady state was achieved, the reaction products were analyzed with a SP3420 gas chromatograph (GC) installed with a flame ionization detector and a PONA capillary column (50 m × 0.2 mm).

2.6. Diffusivity measurements

The thermogravimetric measurements were carried out in a Mettler Toledo TGA/SDTA851e instrument by using a modified thermogravimetric analysis system with online monitoring of mass changes. In each test, about 10 mg of the sample of 60 mesh in size was loaded into the instrument. The calcined sample was pretreated at 723 K in a He atmosphere for 1 h to remove adsorbed impurities, and the absence of impurities during this procedure was indicated by the constant weight of the sample. Thereafter, the sample was cooled to 383 K. The diffusivity measurement was initiated by replacing the He stream with a known amount of gaseous mixture consisting of 2,4-dimethylhexane and He controlled through a precalibrated mass flowmeter. The feed was maintained until the sample was equilibrated as indicated by reaching a constant mass.

3. Results and discussion

3.1. XRD and SEM characterizations

The XRD patterns of the two calcined molecular sieves are shown in Fig. 1. The characteristic peaks at $2\theta = 8.06°, 9.44°, 20.36°, 21.09°, 22.10°, 22.48°$, and $22.74°$ attributed to the typical SAPO-11 phase with AEL structure [24,25] appear in the XRD patterns of the

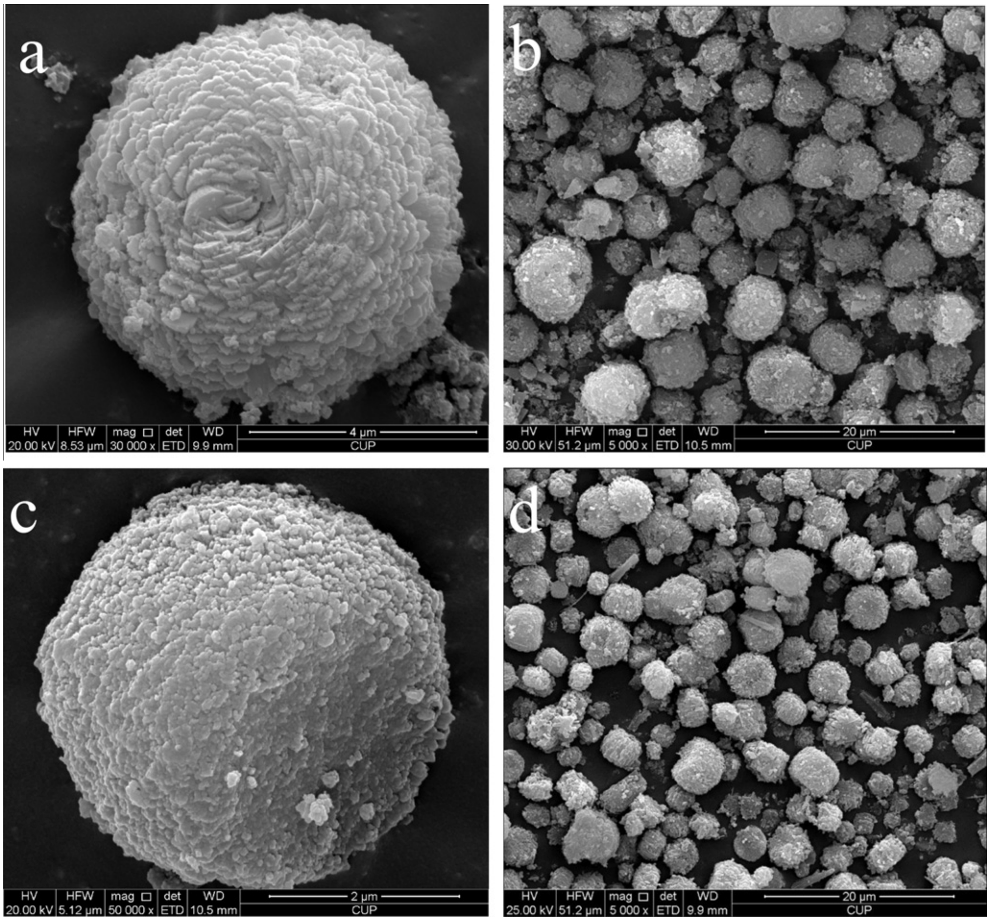

Fig. 2. SEM images of the calcined H-SAPO-11 (a and b) and H-SAPO-11-HI (c and d) molecular sieves.

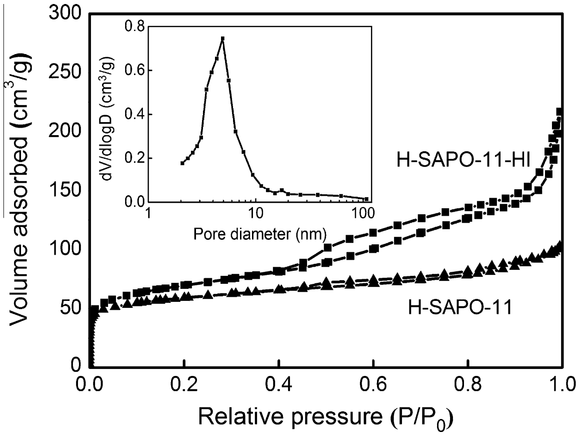

Fig. 3. N_2 adsorption–desorption isotherms of the calcined H-SAPO-11 and H-SAPO-11-HI molecular sieves and pore-size distribution curve of calcined H-SAPO-11-HI (inset).

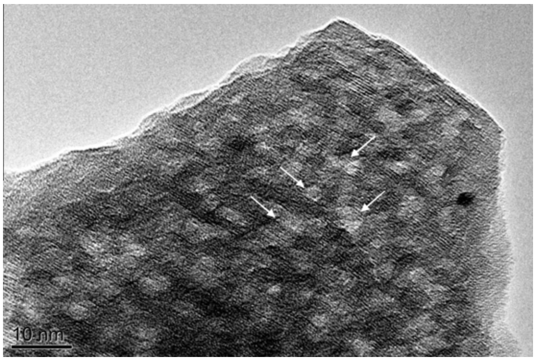

Fig. 4. HRTEM image of the calcined H-SAPO-11-HI molecular sieve with intracrystal mesopores.

H-SAPO-11 and H-SAPO-11-HI molecular sieves, indicating that the involvement of TDPA in the synthesis system commendably preserves the crystal structure of SAPO-11. No additional peaks are observed, showing that the two molecular sieves are free from phase impurities.

The SEM images of the two calcined molecular sieves are presented in Fig. 2. Without amorphous phases, the microporous H-SAPO-11 phase is present in the form of ca. 6-μm pseudospherical aggregates consisting of ca. 600-nm cubic plate monocrystals (Fig. 2a and b), while the H-SAPO-11-HI phase is present in the form of ca. 4-μm spherical aggregates consisting of ca. 350-nm pseudospherical monocrystals (Fig. 2c and d).

3.2. N_2 adsorption–desorption and HRTEM characterizations

The N_2 adsorption–desorption isotherms of the two calcined molecular sieves and the pore-size distribution curve of calcined H-SAPO-11-HI are presented in Fig. 3. H-SAPO-11 has an isotherm typical for pure microporous materials, while H-SAPO-11-HI has an isotherm with not only the characteristics of microporous materials at the low relative pressure P/P_0 but also those of mesoporous materials with a type IV hysteresis at the high relative pressure P/P_0. Correspondingly, H-SAPO-11-HI shows the most probable mesopore diameter at about 5.0 nm, as shown in the inset of Fig. 3.

The pore structure parameters of the two calcined molecular sieves given in Table 1 show that with respect to those of H-SAPO-11, the BET and external surface areas of H-SAPO-11-HI increase by about 34% and 158%, respectively, whereas the microporous surface area of H-SAPO-11-HI decreases only by about 17%. This suggests that the addition of TDPA not only transforms part of micropores into mesopores but also generates new mesopores. Compared with H-SAPO-11, H-SAPO-11-HI has a slightly lower micropore volume and a much higher mesopore volume, demonstrating its well-developed mesopores.

To further demonstrate the bimodal pore structure of calcined H-SAPO-11-HI, HRTEM characterization was performed and the results are shown in Fig. 4. The ordered lattice fringes of micropores of about 0.6 nm in size typical for the conventional SAPO-11 [26] can be explicitly observed in Fig. 4, indicating that the observed region is a single crystal rather than an aggregate of nanocrystals. Moreover, the mesopores with the size of 4–7 nm (the white area with higher contrast, pointed out by the white arrows in Fig. 4) completely run through the micropore fringes, confirming the existence of well-developed intracrystal mesopores that are partially continuous and open to the external surface of the crystal. The formation of these intracrystal mesopores can be illustrated as follows: as shown in Scheme 1, the P atoms in TDPA participate in the formation of microporous SAPO-11 frameworks directed by DPA, so the long alkyl groups bonded with these P atoms are attached to microporous SAPO-11 frameworks and implanted between micropores, inducing the meso-scale intracrystal spaces. The subsequent calcination of the obtained material removes the long alkyl groups and leads to the formation of uniform intracrystal mesopores. Thus, a novel SAPO-11 structure with hierarchical micro-mesopores is created, which will be further expounded by the following characterizations.

3.3. ^{27}Al, ^{31}P, and ^{29}Si MAS NMR and IR characterizations

The ^{27}Al, ^{31}P, and ^{29}Si MAS NMR spectra of the two calcined molecular sieves are shown in Fig. 5. The ^{27}Al MAS NMR spectra show a sharp peak at 37 ppm assigned to the tetrahedral aluminum in the framework and a low peak at 8 ppm assigned to the five-coordinated aluminum [27,28] (Fig. 5a). The ^{31}P MAS NMR spectra display one single peak at −29 ppm assigned to the tetrahedral P in the framework [29] (Fig. 5b). The results in Fig. 5a and b indicate that H-SAPO-11-HI possesses fully condensed crystalline frameworks as in the case of conventional SAPO-11 crystals, and all the P atoms in H-SAPO-11-HI including those bonded to long alkyl groups of TDPA exist in the form of tetrahedrally coordinated P atoms in the frameworks.

In the ^{29}Si MAS NMR spectra (Fig. 5c), both H-SAPO-11 and H-SAPO-11-HI exhibit a broad resonance curve in the range of −86 to −113 ppm reflecting the contributions of different framework Si species. By considering the individual contributions of the five peaks located at ca. −86, −95, −101, −106, and −112 ppm ascribed to Si (4Al), Si (3Al, 1Si), Si (2Al, 2Si), Si (Al, 3Si), and Si (4Si) species [30], respectively, the experimentally determined ^{29}Si MAS NMR spectra of the two molecular sieves were simulated by using Gaussian

Table 1
Pore structure parameters of the two calcined molecular sieves.

Sample	S_{BET} (m^2/g)	S_{micro} (m^2/g)	S_{Ext} (m^2/g)	V_{micro} (cm^3/g)	V_{Meso} (cm^3/g)	V_{Total} (cm^3/g)
H-SAPO-11	219	155	64	0.08	0.06	0.14
H-SAPO-11-HI	293	128	165	0.07	0.31	0.38

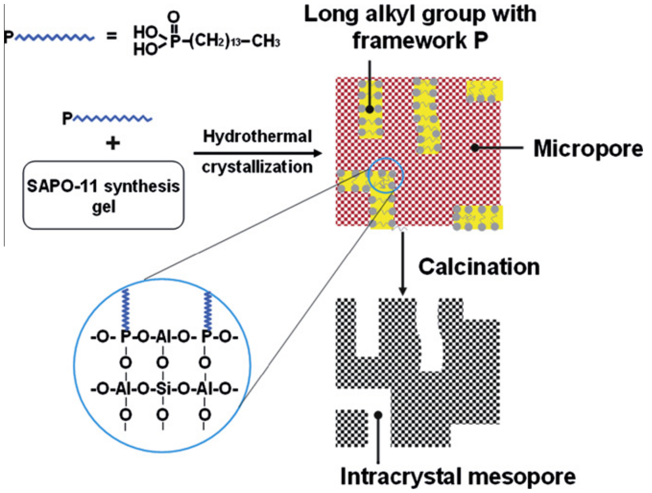

Scheme 1. The proposed synthesis strategy for generating intracrystal mesopores in microporous SAPO-11 monocrystal.

curves, and the results are shown in Table 2. It can be seen that the amount of Si (*n*Al, 4-*n*Si) with $n = 1–3$ for H-SAPO-11-HI is much higher than that for H-SAPO-11, because of the great decrease in the size of the silica domains in the TDPA-containing synthesis system. For SAPO molecular sieves, when Si atoms are just introduced into the framework of AlPO by the substitution of one Si for one P, the SAPO region with Si (4Al) will be formed. If some Si atoms are also introduced by the substitution of two Si for one P and one Al to form the Si domains in addition to the above substitution, the Si (*n*Al, 4-*n*Si) with $n = 1–3$ resulting from the border of Si domains will be formed [31,32]. Thus, in the case of the same Si/Al ratio, the smaller Si domains can produce more borders and thereby more Si (*n*Al, 4-*n*Si) with $n = 1–3$. The above analyses confirm that introducing TDPA into the conventional SAPO-11 synthesis remarkably benefits the dispersion of Si domains to generate more Si (*n*Al, 4-*n*Si) with $n = 1–3$.

The IR spectra of the two uncalcined molecular sieves are shown in Fig. 6. Distinctly different from H-SAPO-11, H-SAPO-11-HI exhibits the bands at 2957, 2924, and 2850 cm^{-1} assigned to the characteristic stretching vibration of CH groups originating from the long alkyl chains of TDPA [33–35], indicating the well-retained alkyl chains of TDPA in the SAPO-11 structure. Since the P atoms in the introduced TDPA are located in the SAPO-11 frameworks as confirmed by the ^{31}P MAS NMR characterization results, the well-retained long alkyl groups bonded with these P atoms are embedded into the microporous SAPO-11 frameworks by the bridging effect of these P atoms and thus intracrystal mesopores are produced after calcination, supporting the proposed synthesis strategy in Scheme 1.

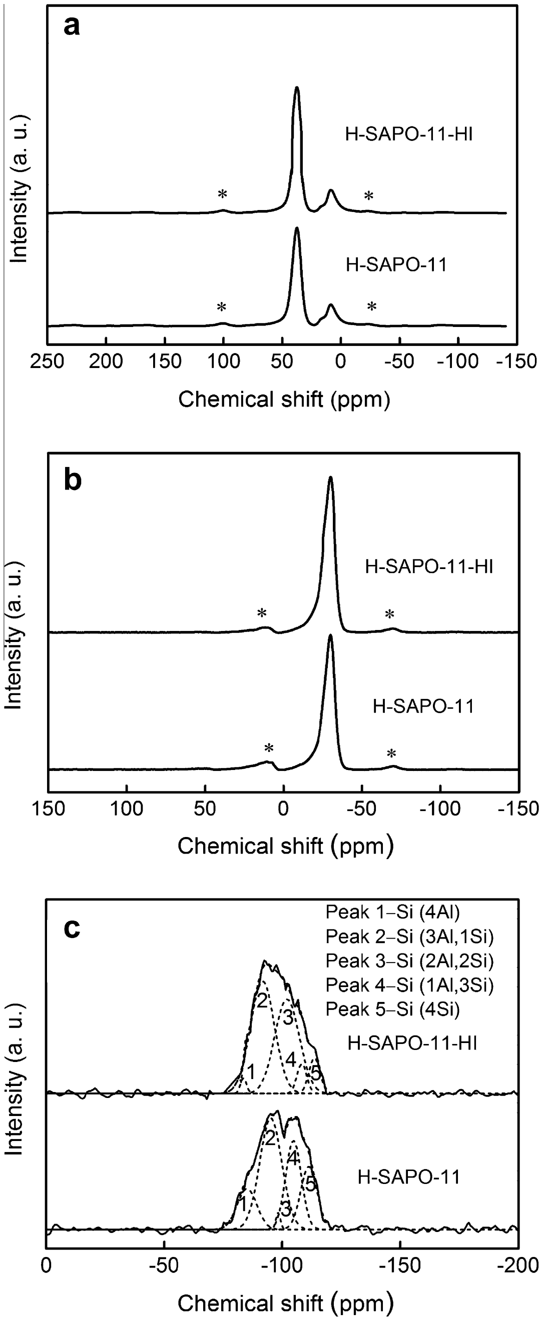

Fig. 5. ^{27}Al (a), ^{31}P (b) and ^{29}Si (c) MAS NMR spectra of the calcined H-SAPO-11 and H-SAPO-11-HI molecular sieves; asterisks (∗) correspond to spinning side bands.

3.4. TG and Py-IR characterizations

The TG curves of the two uncalcined molecular sieves are shown in Fig. 7. The weight loss below 473 K corresponds to the removal of physically adsorbed water, while the loss between 473 and 1073 K mainly corresponds to the decomposition of the organic template DPA and the organophosphorus TDPA. It is noted that the weight loss between 723 and 1073 K for H-SAPO-11-HI is larger than that for H-SAPO-11, attributed to the decomposition of TDPA in view of the identical amount of DPA introduced in synthesizing H-SAPO-11-HI and H-SAPO-11. It is the decomposition of TDPA that renders H-SAPO-11-HI to have a larger pore volume and more complex pore structure compared with H-SAPO-11. The decomposition temperature of TDPA in H-SAPO-11-HI is much higher than that (473 K) for TDPA itself [36], signifying that TDPA participates in the synthesis reactions of H-SAPO-11-HI and thus its decomposition is more difficult due to its interaction with Si and Al atoms.

The pyridine-adsorbed IR spectra of the two calcined molecular sieves in the wavenumber range of 1600–1400 cm^{-1} are shown in Fig. 8. The bands at 1545 and 1455 cm^{-1} correspond to those specific to the pyridine molecules chemisorbed on Brönsted (B) and Lewis (L) acid sites, respectively [37]. Total L acidity and total B acidity, and medium and strong L acidity and medium and strong B acidity can be calculated from the spectra of pyridine adsorption at 473 and 573 K, respectively. The quantitative acidity analysis

Table 2
Deconvolution results of the ^{29}Si MAS NMR spectra of the two calcined molecular sieves based on the normalized peak areas of the different Si species.

Sample	Si (4Al) (%)	Si (3Al, 1Si) (%)	Si (2Al, 2Si) (%)	Si (1Al, 3Si) (%)	Si (4Si) (%)
H-SAPO-11	10.5	40.1	2.3	25.4	21.7
H-SAPO-11-HI	2.6	46.5	41.7	3.9	5.3

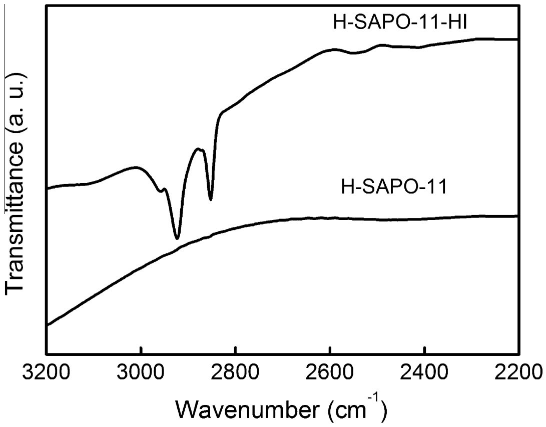

Fig. 6. IR spectra of the uncalcined H-SAPO-11 and H-SAPO-11-HI molecular sieves.

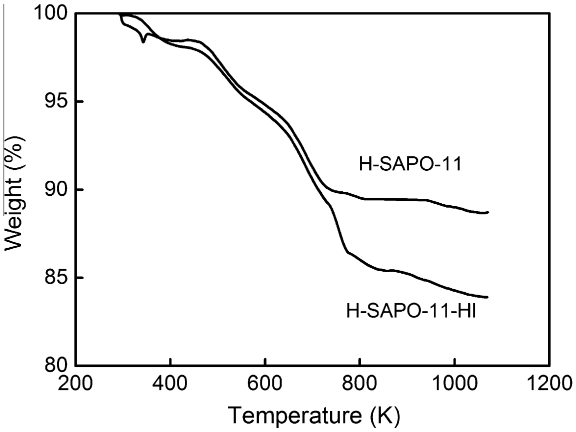

Fig. 7. TG curves of the uncalcined H-SAPO-11 and H-SAPO-11-HI molecular sieves.

results can be obtained according to the method described elsewhere [38]. The difference between total acidity and medium and strong acidity stands for weak acidity. As shown in Table 3, compared with H-SAPO-11, H-SAPO-11-HI has the similar amounts of weak L acid sites and medium and strong L acid sites, the relatively more amount of weak B acid sites, and the much higher amount of medium and strong B acid sites.

The much more B acid sites with the medium and strong acidity in H-SAPO-11-HI can be explained as follows: for SAPO molecular sieves, B acid sites result from the SAPO region and the border of Si domains, but those from the latter (Si (nAl, 4-nSi) with n = 1–3) differ from those from the former (Si (4Al)) [39]. The B acid sites at the border of Si domains possess higher acid strength than those in the SAPO region [39]. Therefore, the medium and strong B acid sites originating from the border of Si domains correspond to Si (nAl, 4-nSi) with n = 1–3 in the framework of SAPO-11. Because the above ^{29}Si MAS NMR results have verified that H-SAPO-11-HI has much smaller Si domains and thus much more Si (nAl, 4-nSi) with n = 1–3 compared with H-SAPO-11, H-SAPO-11-HI presents the much more medium and strong B acid sites.

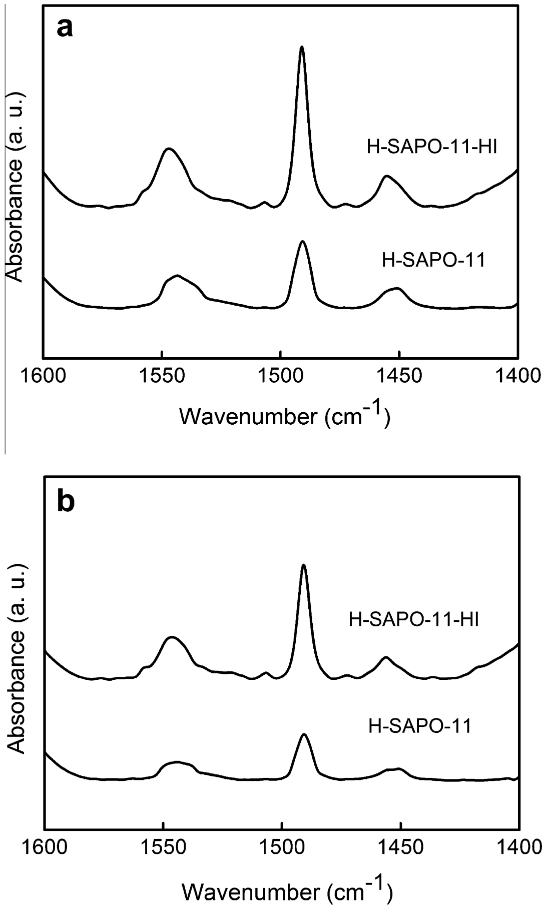

Fig. 8. IR spectra of pyridine adsorbed on the calcined H-SAPO-11 and H-SAPO-11-HI molecular sieves at (a) 473 K and (b) 573 K.

The results in Table 3 also display that the incorporation of 1.0 wt% Pt into the two molecular sieves leads to the decrease in B acidity and the increase in L acidity, but the acidity difference between the two catalysts is very similar to that between the two molecular sieves without Pt loading.

3.5. Diffusivity and metal dispersion

In order to investigate the effect of the mesopore formation on the improvement of mass transfer ability in the SAPO-11 framework, the diffusivity measurement of 2,4-dimethylhexane was carried out. For an isothermal system, a solution to the transient diffusion equation for a spherical particle is [40]

$$\Delta m_t = \Delta m_\infty \left[1 - \frac{6}{\pi^2} \sum_{j=1}^{\infty} \frac{1}{j^2} \exp\left(-\frac{j^2 \pi^2 D t}{R^2} \right) \right] \tag{1}$$

where Δm_t is the mass increase at time t, R is the effective diffusion length within the particle, and D is the diffusivity. The presence of mesopores in the particle will lead to a shorter diffusion length.

Table 3
Acid type distributions of the two calcined molecular sieves and corresponding catalysts obtained by the Py-IR analysis.

Sample	Acidity (μmol/g)			
	Weak acid sites		Medium and strong acid sites	
	L	B	L	B
H-SAPO-11	33.6	62.3	29.5	46.1
H-SAPO-11-HI	37.8	72.7	34.2	131.2
Pt/H-SAPO-11	43.5	56.0	31.7	37.5
Pt/H-SAPO-11-HI	48.4	64.9	37.2	124.6

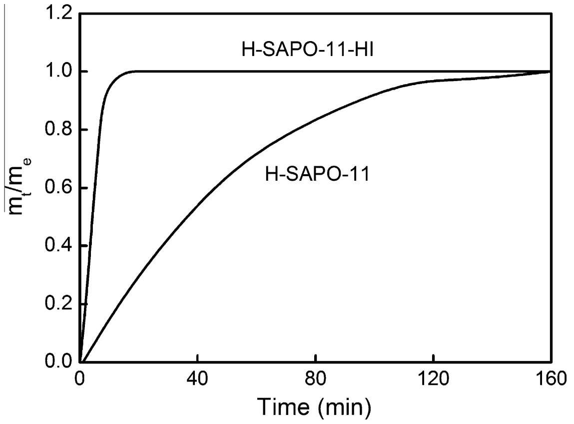

Fig. 9. Diffusion of 2,4-dimethylhexane in the calcined H-SAPO-11 and H-SAPO-11-HI molecular sieves.

When the adsorption and desorption reach equilibrium, the solution reduces to the approximate form [41]

$$\Delta m_t = \Delta m_\infty \left[1 - \frac{6}{\pi^2}\exp\left(\frac{-\pi^2 Dt}{R^2}\right)\right] \qquad (2)$$

Therefore, there is a linear relationship between $\ln\left(1 - \frac{\Delta m_t}{\Delta m_\infty}\right)$ and t, and the slope of this straight line yields directly the diffusion time constant D/R^2 that can be considered as a parameter for assessing the diffusion performance of different samples [42].

Fig. 9 shows the relation between $\frac{m_t}{m_e}$ and diffusion time t, where m_t and m_e denote the amounts of 2,4-dimethylhexane adsorbed at time t and at adsorption equilibrium, respectively. It can be seen that the adsorption rate of 2,4-dimethylhexane into H-SAPO-11-HI is much higher than into H-SAPO-11. The calculated values of the diffusion time constant D/R^2 are $10.88 \times 10^{-4}\,s^{-1}$ for H-SAPO-11-HI and $0.96 \times 10^{-4}\,s^{-1}$ for H-SAPO-11, respectively, demonstrating the dramatic effect of mesopores in H-SAPO-11-HI on enhancing the diffusion of di-branched C_8 isomers.

The metal dispersions determined by hydrogen adsorption are 51% for Pt/H-SAPO-11 and 52% for Pt/H-SAPO-11-HI, respectively, indicating the almost identical Pt dispersion on the two catalysts.

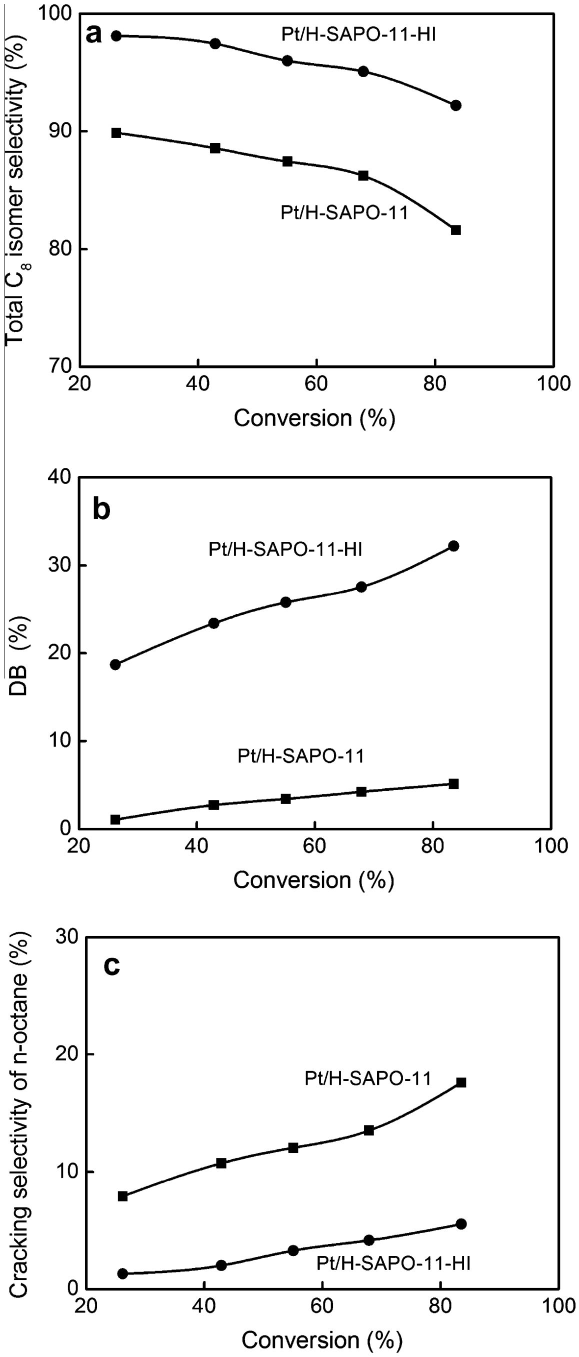

Fig. 10. Total C_8 isomer selectivity (a), percentage of di-branched C_8 isomers in total C_8 isomers denoted as DB (b), and cracking selectivity of *n*-octane (c) versus *n*-octane conversion over the Pt/H-SAPO-11 and Pt/H-SAPO-11-HI catalysts.

3.6. Catalytic activities

The isomerization results of the Pt/H-SAPO-11 and Pt/H-SAPO-11-HI catalysts are shown in Fig. 10. With the increasing *n*-octane conversion, the total C_8 isomer selectivities obtained over the two catalysts decrease, while the values of DB, defined as the percentage of di-branched C_8 isomers in total C_8 isomers, and the cracking selectivities of *n*-octane increase. This indicates that the high conversion can efficiently promote the generation of di-branched C_8 isomers, but simultaneously enhance the cracking side-reactions that lead to the decreased total selectivity for C_8 isomers. It is known that the bottleneck in the skeletal isomerization of hydrocarbons lies in the contradiction between high-efficient isomerization and minimal cracking [22], so it is desirable to search for a catalyst that can efficiently reconcile this contradiction. Compared with the Pt/H-SAPO-11 catalyst, the Pt/H-SAPO-11-HI catalyst has the much higher selectivity to total C_8 isomers, the higher DB value, and the much lower cracking selectivity at different conversions of *n*-octane, demonstrating its remarkable advantage for the skeletal isomerization of hydrocarbons.

The results of product selectivity in Table 4 show that Pt/H-SAPO-11 has the high selectivities to 2-methylheptane (2-MC_7) and 3-methylheptane (3-MC_7) because the ring opening of the C_8 protonated cyclopropane (PCP) intermediate at terminal position

Table 4
Results of *n*-octane isomerization over the two catalysts.

	Pt/H-SAPO-11	Pt/H-SAPO-11-HI
k^a (10^{-6} mol g^{-1} s^{-1})	5.1	33.2
TOF^b (10^{-2} s^{-1})	5.5	17.5
$S_{MB}{}^c$ (%)	86.1	74.0
$S_{DB}{}^c$ (%)	2.4	23.9
iC_4/nC_4	0.58	1.5
iC_5/nC_5	0.51	1.1
$(C_3 + C_5)/2C_4$	0.70	0.68
PS^c (%)		
2-MC$_7$	40.6	30.0
3-MC$_7$	36.8	36.1
4-MC$_7$	8.7	7.9
2,2-DMC$_6$	0.0	1.5
2,3-DMC$_6$	0.2	2.6
2,4-DMC$_6$	0.6	9.5
2,5-DMC$_6$	1.6	10.3
Cracking of *n*-octane	11.5	2.1

[a] Reaction rate constant obtained by assuming a pseudo-first-order reaction for *n*-octane isomerization at 593 K, 1.5 MPa, a H_2/octane volumetric ratio of 400, and 12.0 WHSV.

[b] Number of reacted *n*-octane molecules per second and per B acid site.

[c] S_{MB}, S_{DB}, and *PS* correspond to the total selectivity for mono-branched C_8 isomers, the total selectivity for di-branched C_8 isomers, and the product selectivity, respectively, at 43% conversion of *n*-octane.

favors the formation of 2-MC$_7$ and 3-MC$_7$ among the other mono-branched isomers [43]. The higher selectivity to 2-MC$_7$ than to 3-MC$_7$ can be explained by the product shape selectivity in Pt/H-SAPO-11, and the very low selectivities to the different di-branched C_8 isomers in Pt/H-SAPO-11 can be attributed to their larger size than the pore diameter of H-SAPO-11 [30]. Compared with Pt/H-SAPO-11, Pt/H-SAPO-11-HI presents the much higher selectivities to the di-branched C_8 isomers with the order of 2,5-dimethylhexane (2,5 DMC$_6$) > 2,4-dimethylhexane (2,4 DMC$_6$) > 2,3-dimethylhexane (2,3 DMC$_6$) > 2,2-dimethylhexane (2,2 DMC$_6$). These di-branched C_8 isomers obtained over Pt/H-SAPO-11-HI originate from the further skeleton isomerization of 2-MC$_7$ formed [44], as evidenced by the lower product selectivity to 2-MC$_7$ over Pt/H-SAPO-11-HI than over Pt/H-SAPO-11. In addition, Pt/H-SAPO-11-HI has the much lower cracking selectivity of *n*-octane and the higher ratios of iC_4/nC_4 and iC_5/nC_5 than Pt/H-SAPO-11, indicating that the total content of the *n*-octane cracking products is much lower over Pt/H-SAPO-11-HI, and in these cracking products, the more branched products from the cracking of di-branched C_8 isomers are formed.

In view of the almost identical Pt dispersion on the two catalysts as mentioned in the above characterizations, it is concluded that the isomerization results are not influenced by the metal function. Thus, the catalytic activities of the two catalysts are considered to depend upon their pore structure and acidity, as will be discussed below.

As for Pt/H-SAPO-11, *n*-octane with a critical molecular diameter of 0.49 nm [29] first experiences dehydrogenation on Pt centers, and then the formed olefin molecules are converted to the precursors of mono-branched C_8 isomers with a critical molecular diameter of 0.56 nm [29]. The longer pore channels of the conventional H-SAPO-11 lead to the increased residence time of the carbenium ions of mono-branched C_8 isomers and thus result in their further cracking on medium and strong acid sites. Due to the larger size of di-branched C_8 isomers (0.71 nm) [22] than the pore diameter (0.63 nm) of microporous H-SAPO-11 [45], only a minor portion of di-branched C_8 isomers can be formed at the pore mouths rather than in the microporous channels according to the "pore mouth and key lock" concept [46]. Therefore, Pt/H-SAPO-11 shows the higher cracking selectivity and the lower di-branched C_8 isomer ratio, as shown in Fig. 10 and Table 4.

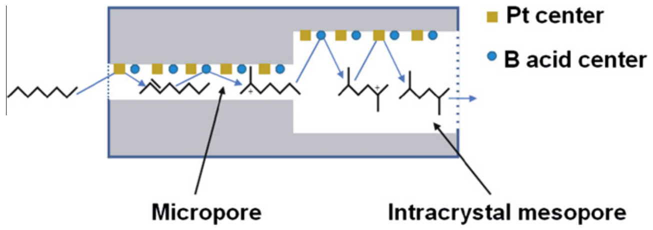

Scheme 2. Reaction and diffusion pathways for *n*-octane isomerization in the pore channels of H-SAPO-11-HI monocrystal.

The results of the ^{31}P MAS NMR, IR and TG characterizations have demonstrated that the P atoms in the introduced organophosphorus TDPA are located in the SAPO-11 frameworks, and the well-retained long alkyl groups bonded with these P atoms are embedded into the microporous SAPO-11 frameworks, so H-SAPO-11-HI has the interconnected micro- and meso-porous structure, as evidenced by the HRTEM and N_2 adsorption–desorption characterization results. Therefore, the excellent isomerization performance of Pt/H-SAPO-11-HI is attributed to the hierarchical pore structure of H-SAPO-11-HI that provides a unique reaction path to octane isomerization (Scheme 2). First, the olefin molecules formed from the dehydrogenation of *n*-octane on Pt centers enter the short micropores intersecting with intracrystal mesopores and are subsequently converted into the carbenium ions of mono-branched (MB) C_8 isomers on the active B acid centers; then, these carbenium ions rapidly depart from the short microporous channels and diffuse into the interconnected intracrystal mesopores where their di-branched (DB) isomerization is finished without steric hindrance; finally, the di-branched C_8 isomers generated by the hydrogenation of their carbenium ions on Pt centers can quickly reach the external surface and diffuse into the surrounding environment. The open and interconnected micro–mesoporous channels in H-SAPO-11-HI guarantee the much higher di-branched C_8 isomer ratio and the much lower cracking selectivity over Pt/H-SAPO-11-HI than those over Pt/H-SAPO-11, as shown in Fig. 10 and Table 4.

The results of the ^{29}Si MAS NMR and Py-IR characterizations for the two molecular sieves have shown that H-SAPO-11-HI has more small Si domains and thus more medium and strong B acid sites compared with H-SAPO-11. The medium and strong B acid sites are considered as the active sites for the skeletal rearrangement (isomerization) and C–C bond cracking of hydrocarbons [47], so the increase in their number can efficiently promote not only the mono- and di-branched sequential isomerization of *n*-octane but also accelerate the *n*-octane cracking. However, Pt/H-SAPO-11-HI with more medium and strong B acid sites presents not only a higher activity (reflected by the higher reaction rate constant and TOF (turn-over frequency)) and a better di-branched isomer selectivity, but also a lower cracking selectivity compared with Pt/H-SAPO-11 at the same conversion of *n*-octane (Table 4). This salient feature can be ascribed to the fact that the superior mass transport in the interpenetrating micro–mesoporous architecture of Pt/H-SAPO-11-HI suppresses the *n*-octane cracking, in addition to the promoting effect of medium and strong B acid sites on the skeletal isomerization of *n*-octane.

4. Conclusions

An alkylphosphonic acid- and small amine-templated hydrothermal method for synthesizing hierarchical SAPO-11 molecular sieves was proposed, and the skeleton isomerization of *n*-octane was selected as the model reaction to assess its advantages. The results showed that the involvement of tetradecylphosphoric acid (TDPA) in the conventional SAPO-11 synthesis system commendably preserved the crystal structure of SAPO-11 and produced a hierarchical SAPO-11 molecular sieve with interconnected micro- and meso-pores. Compared with the conventional SAPO-11, this hierarchical SAPO-11 had much higher external surface and mesoporous volume with the intracrystal mesopores of 4–7 nm and more medium and strong Brönsted acid sites active for hydrocarbon isomerization. The well-developed pore structure of the hierarchical SAPO-11 alleviated the diffusion hindrance existing in microporous channels of the conventional SAPO-11 and efficiently restrained the hydrocarbon cracking on medium and strong acid sites, endowing the corresponding catalyst with excellent dibranched isomer selectivity in the long-chain paraffin isomerization.

Acknowledgments

This work was supported by the National Basic Research Program of China (Grant 2010CB226905), the Program for New Century Excellent Talents in University (Grant NCET-09-0763), the National Natural Science Foundation of China (Grants 21076228 and 20825621), and the Nova Program of Beijing (Grant 2007B073).

References

[1] J. Čejka, S. Mintova, Catal. Rev. 49 (2007) 457.
[2] M.E. Davis, Nature 417 (2002) 813.
[3] J. Pérez-Ramírez, F. Kapteijn, J.C. Groen, A. Domenech, G. Mul, J.A. Moulijn, J. Catal. 214 (2003) 33.
[4] B.J. Schoeman, J. Sterte, J.E. Otterstedt, Zeolites 14 (1994) 110.
[5] A. Corma, M. Diaz-Cabanas, J. Martinez-Triguero, F. Rey, J. Rius, Nature 418 (2002) 514.
[6] X. Zou, T. Conradsson, M. Klingstedt, M.S. Dadachov, M. ÓKeeffe, Nature 437 (2005) 716.
[7] C.T. Kresge, M.E. Leonowicz, W.J. Roth, J.C. Vartuli, J.S. Beck, Nature 359 (1992) 710.
[8] D. Zhao, J. Feng, Q. Huo, N. Melosh, G.H. Fredrickson, B.F. Chmelka, G.D. Stucky, Science 279 (1998) 548.
[9] X. Meng, F. Nawaz, F. Xiao, Nano Today 4 (2009) 292.
[10] M. Hartmann, Angew. Chem. Int. Ed. 43 (2004) 5880.
[11] S. van Donk, A.H. Janssen, J.H. Bitter, K.P. de Jong, Catal. Rev. 45 (2003) 297.
[12] K. Egeblad, C.H. Christensen, M. Kustova, C.H. Christensen, Chem. Mater. 20 (2008) 946.
[13] C.J.H. Jacobsen, C. Madsen, J. Houzvicka, I. Schmidt, A. Carlsson, J. Am. Chem. Soc. 122 (2000) 7116.
[14] C.H. Christensen, I. Schmidt, A. Carlsson, K. Johannsen, K. Herbst, J. Am. Chem. Soc. 127 (2005) 8098.
[15] F. Xiao, L. Wang, C. Yin, K. Lin, Y. Di, J. Li, R. Xu, D. Su, R. Schlögl, T. Yokoi, T. Tatsumi, Angew. Chem. Int. Ed. 45 (2006) 3090.
[16] D.H. Park, S.S. Kim, H. Wang, T.J. Pinnavaia, M.C. Papapetrou, A.A. Lappas, K.S. Triantafyllidis, Angew. Chem. Int. Ed. 48 (2009) 7645.
[17] V. Valtchev, M. Smaihi, A. Faust, L. Vidal, Angew. Chem. Int. Ed. 42 (2003) 2782.
[18] M. Choi, H.S. Cho, R. Srivastava, C. Venkatesan, D.H. Choi, R. Ryoo, Nat. Mater. 5 (2006) 718.
[19] H. Wang, T.J. Pinnavaia, Angew. Chem. Int. Ed. 45 (2006) 7603.
[20] M. Choi, R. Srivastava, R. Ryoo, Chem. Commun. 42 (2006) 4380.
[21] N. Danilina, F. Krumeich, J.A. van Bokhoven, J. Catal. 272 (2010) 37.
[22] V.M. Akhmedov, S.H. Al-Khowaiter, Catal. Rev. 49 (2007) 33.
[23] P. Mériaudeau, V.A. Tuan, G. Sapaly, V.T. Nghiem, S.Y. Lai, L.N. Hung, C. Naccache, Catal. Today 49 (1999) 285.
[24] Y. Fan, D. Lei, G. Shi, X. Bao, Catal. Today 114 (2006) 388.
[25] S.T. Wilson, B.M. Lok, E.M. Flanigen, US Patent 4310440, To Union Carbide Corporation, 1982.
[26] J.M. Campelo, F. Lafont, J.M. Marinas, Appl. Catal. A – Gen. 152 (1997) 53.
[27] D. Zhou, J. Xu, J. Yu, L. Chen, F. Deng, R. Xu, J. Phys. Chem. B 110 (2006) 2131.
[28] C.A. Fyfe, K.C. Wong-Moon, Y. Huang, Zeolites 16 (1996) 50.
[29] P. Mériaudeau, V.A. Tuan, V.T. Nghiem, S.Y. Lai, L.N. Hung, C. Naccache, J. Catal. 169 (1997) 55.
[30] P. Mériaudeau, V.A. Tuan, F. Lefebvre, V.T. Nghiem, C. Naccache, Micropor. Mesopor. Mater. 22 (1998) 435.
[31] T. Masukawa, T. Komatsu, T. Yashima, Zeolites 18 (1997) 10.
[32] J.A. Martens, P.J. Grobet, P.A. Jacobs, J. Catal. 126 (1990) 299.
[33] H. Tanaka, M. Chikazawa, J. Mater. Chem. 9 (1999) 2923.
[34] R. Luschtinetz, G. Seifert, E. Jaehne, H.J.P. Adler, Macromol. Symp. 254 (2007) 248.
[35] T. Ma, X. Zhang, Z. Yuan, J. Phys. Chem. C 113 (2009) 12854.
[36] M. Fröba, M. Tiemann, Chem. Mater. 10 (1998) 3475.
[37] J.A.Z. Pieterse, S. Veefkind-Reyes, K. Seshan, L. Domokos, J.A. Lercher, J. Catal. 187 (1999) 518.
[38] C.A. Emeis, J. Catal. 141 (1993) 347.
[39] T. Blasco, A. Chica, A. Corma, W.J. Murphy, J. Agúndez-Rodríguez, J. Pérez-Pariente, J. Catal. 242 (2006) 153.
[40] J. Crank, in: The Mathematics of Diffusion, Oxford Press, London, 1975.
[41] J. Karger, D.M. Ruthven, in: Diffusion in Zeolites and Other Microporous Solids, John Wiley, New York, 1992.
[42] X. Li, R. Prins, J.A. van Bokhoven, J. Catal. 262 (2009) 257.
[43] S. Ernst, J. Weitkamp, J.A. Martens, P.A. Jacobs, Appl. Catal. 48 (1989) 137.
[44] W. Zhang, P.G. Smirniotis, J. Catal. 182 (1999) 400.
[45] M. Höchtl, A. Jentys, H. Vinek, J. Catal. 190 (2000) 419.
[46] M.C. Claude, G. Vanbutsele, J.A. Martens, J. Catal. 203 (2001) 213.
[47] X. Huang, L. Wang, L. Kong, Q. Li, Appl. Catal. A – Gen. 253 (2003) 461.